Transparent LiOH-doped magnesium aluminate spinel produced by spark plasma sintering: Effects of heating rate and dopant concentration

Václav Pouchlý [a,b,*], Ali Talimian [c], Jaroslav Kaštyl [d], Martin Chvíla [b], Erik Ščasnovič [a,b], Ana M. Betlrán [e], Juan G. Lozano [e,f], Dušan Galusek [c,g]

[a] Central European Institute of Technology, Brno University of Technology, Purkyňova 123, 612 00 Brno, the Czech Republic
[b] Faculty of Mechanical Engineering, Brno University of Technology, Technická 2, 612 00 Brno, the Czech Republic
[c] Centre for Functional and Surface Functionalised Glass, Alexander Dubček University of Trenčín, Študentská 2, 91150 Trenčín, Slovakia
[d] TESCAN Brno, s.r.o., Libušina třída 1, 623 00 Brno, the Czech Republic
[e] Departamento de Ingeniería y Ciencia de los Materiales y del Transporte, Escuela Politécnica Superior, Universidad de Sevilla, 41011 Seville Spain
[f] Departamento de Ingeniería y Ciencia de los Materiales y del Transporte, Escuela Técnica Superior de Ingeniería, Universidad de Sevilla, 41092 Seville Spain
[g] Joint Glass Centre of the IIC SAS, TnUAD and FChPT STU, Študentská 2, 91150 Trenčín, Slovakia

ARTICLE INFO

ABSTRACT

The effects of LiOH doping of magnesium aluminate spinel powders and various Spark Plasma Sintering (SPS) schedules on densification behavior and final transparency of polycrystalline magnesium aluminate spinel were studied. Two commercial magnesium aluminate spinel powders, with different specific surface areas, were doped with up to 0.6 wt% of LiOH and consolidated using SPS with slow (2.75 °C/min) and fast (100 °C/min) heating rates. The slow heating rate was optimal for undoped magnesium aluminate spinel (LiOH-free) with the best real in-line transmittance (RIT) of 84.8% (measured at 633 nm on a disc 0.8 mm thick). For the magnesium aluminate spinel doped with 0.3 wt% of LiOH, the fast heating rate was beneficial, and an RIT of 76.5% was achieved. μ-Raman analysis confirmed that the addition of LiOH suppressed carbon contamination.

1. Introduction

Owing to the high transparency over a wide range of wavelengths, good mechanical properties, and chemical durability, magnesium aluminate spinel (hereafter termed "spinel") is a potential candidate for various engineering applications, from optical lenses to covers for optical sensors to face shields [1–4]. In principle, transparent polycrystalline magnesium aluminate spinel can be obtained by producing a highly dense body free from scattering centers such as impurities or pores. However, the fabrication of transparent spinel bodies using conventional ceramic powder processing methods is challenging and requires extreme care. Impurities play detrimental roles in the transparency of samples and, thus, highly pure powders should be used. Even then, conventional sintering methods often fail to densify spinel and eliminate all pores due to the slow diffusion of participating elements [5–8]. Thus, transparent polycrystalline spinel is often fabricated using pressure-assisted sintering techniques such as Hot Pressing (HP), Hot Isostatic Pressing (HIP), or Spark Plasma Sintering (SPS) [3,4,9–11].

Although Spark Plasma Sintering (SPS) enables producing highly

dense and fine-grained ceramics in a short time, carbon contamination introduced from graphite dies, is inevitable in this process [12–14]. Carbon contamination results in the blackening of spinel and reduces the transparency of final bodies [12,14,15]. Significant attention was therefore paid to the reduction or elimination of carbon contamination during spark plasma sintering [12–14,16–19]. So far, the addition of fluoride sintering aids, such as LiF and MnF$_2$, has been considered the most effective method to reduce carbon contamination. Fluoride sintering aids produce a low melting temperature liquid that scavenges the impurities and removes carbon contamination via producing volatile CF$_x$ gasses. [20–24] Furthermore, the liquid produced from the sintering aid promotes densification by facilitating the rearrangement of spinel particles. Despite the benefits of fluoride additives, residual liquid at the grain boundaries can decrease the transparency of the final body [11,22,24]. Nečina and Pabst [25] have shown that the presence of a liquid is not essential for the densification of spinel. Also, lithium hydroxide has been introduced as an alternative sintering aid to lithium fluoride with a similar impact on densification [26]. Although lithium hydroxide produces no liquids during sintering, Li$^+$ ions incorporate into the spinel

---

structure, introduce oxygen vacancies and improve matter diffusion [26, 27]. However, the chemical reactions resulting in the formation of CF_x gasses are not present when LiOH is added.

Carbon contamination can also be avoided by performing two-stage SPS [19]. SPS at a slow heating rate produces isolated pores below a temperature called "critical temperature", where carbon deposition in pores is not thermodynamically favored; consequently, carbon contamination can be minimized [13,28]. However, the two-stage SPS is time-consuming. Adding LiOH promotes spinel densification; thus, isolated pores can be obtained below the critical temperature by careful selection of SPS schedule.

In the present study, SPS is carried out following one of two typical approaches, namely: (i) "*fast*" and (ii) "*slow*" sintering schedules. The fast sintering consists of heating at high heating rates ($> 100\,°C.min^{-1}$) up to the final temperature, followed by a short dwell (a few minutes). The slow sintering is carried out at low heating rates, typically below $5\,°C.min^{-1}$, from temperatures above $1000\,°C$ to the final temperature that is usually lower than the dwell temperature of a fast SPS schedule. While the fast SPS is believed to activate grain boundary diffusion mechanisms and facilitate the rearrangement of particles, the lower temperature of slow SPS guarantees fine microstructure and prevents carbon contamination [29–31]. The addition of sintering aids strongly influences the sintering behavior of ceramics.

So far, there has been no report on using LiOH as a sintering aid to magnesium aluminate spinel to produce transparent bodies using spark plasma sintering. In this work, the effect of LiOH doping and SPS schedule on densification behavior and transparency of commercial $MgAl_2O_4$ powders have been studied. Two spinel powders with small differences in properties were doped with up to 0.6 wt% LiOH and consolidated by spark plasma sintering using various sintering regimes.

2. Experimental

Commercial magnesium-aluminate spinel powders S25CR and S30CR (Baikowski, France) were used as raw materials; the properties of the powders provided by the supplier (except for specific surface area - SSA) are summarized in Table 1. The powders were mixed with 0, 0.3 and 0.6 wt% lithium hydroxide additive. Firstly, the spinel powder was dispersed in isopropanol using an ultrasonic mixer (Sonoplus HD 3400, BANDELIN, Germany). Then, an aqueous solution of lithium hydroxide monohydrate (Sigma-Aldrich, USA) was added to the suspension to prepare a mixture with the required content of LiOH. The mixture was transferred into a rotary evaporator, concentrated under vacuum, and then dried at $120\,°C$ overnight. Lastly, the powder was passed through a sieve with a 0.5 mm mesh. The details of the preparation procedure of doped powders are described elsewhere [26].

2.1. Sintering

Spinel discs were prepared using a Spark Plasma Sintering machine (Dr. Sinter SPS-625, Fuji Electronic Industrial, Japan). For sample preparation, 1.5 g of the powder was poured into a graphite die lined with graphite paper with an inner diameter of 20 mm. The samples were firstly held at $600\,°C$ for 3 min and then heated at $100\,°C.min^{-1}$ up to $1100\,°C$, where the heating schedule continues under "slow" (S) or "fast" (F) SPS schedule. For S heating schedules, the heating rates of 2.50, 2.75, 5.00, 7.50, and $12.50\,°C.min^{-1}$ were applied until the temperature of

1250, 1350 or $1450\,°C$ was reached (with no dwell). The constant pressure of 80 MPa was applied above $800\,°C$ for all samples.

For F heating schedules, the samples were heated at the heating rates of 25, 50, and $100\,°C.min^{-1}$ until 1250, 1300, or $1350\,°C$ with a dwell of 0, 1, 2, 3, 5, 10 or 15 min. A pressure of 80 MPa was applied at different temperatures above $800\,°C$ and kept constant during the whole SPS heating process for all samples. Not all combinations for (S) and (F) schedules were performed; the first combination was chosen by Sequential Design of Experiment (SDoE) analysis leading to various combinations of the lower final temperatures with the higher dwells and vice versa. The temperature was measured by a pyrometer focused into a drilled hole in the center of a graphite die. The sintered discs were heat treated at $725\,°C$ (heating rate $2\,°C.min^{-1}$, 1 h dwell) in a muffle furnace (Clasic 1013 L, Clasic CZ Ltd., the Czech Republic) in ambient atmosphere to burn out the residual carbon.

2.2. Characterization

The density of samples was measured by the Archimedes method in deionized water using an analytical balance (Mettler Toledo AG64, USA). Nine independent measurements were carried out for each sample. The theoretical density of $MgAl_2O_4$ was assumed to be $3.58\,g.cm^{-3}$; the influence of the dopant was considered negligible due to the minute amounts of LiOH.

The specific surface area (SSA) of raw powders was determined by nitrogen sorption performed at 77 K using a sorption analyzer Autosorb iQ (Quantachrome Instruments). Samples were degassed at $180\,°C$ for 3 h under vacuum prior to BET analysis. The SSA was calculated using five points for the P/P_0 range of 0.1–0.3 according to the classical Brunauer-Emmet-Teller (BET) method with a correlation coefficient R= 0.999.

The sintered discs were ground to the nominal thickness of 0.850 mm with a standard deviation of 0.005 mm and then polished to achieve the plane parallel surfaces; finally, the nominal thickness of 0.80 mm was achieved. The roughness of polished surfaces was provided by a contact profilometer (Dektak XT, Bruker, USA) according to EN ISO 4287 and EN ISO 4288 norms. A profilometer tip radius of 2 μm was used. The Ra and Rz roughness parameters were determined as an average of five measurements performed on each sample, and a 95% confidence interval (using t-distribution) was calculated. The data obtained by the profilometer was processed using the software Gwyddion version 2.49.

Real In-line Transmittance (RIT) of SPS samples was measured for two light sources with different wavelengths: the first source with He-Ne laser (Lasos LGK 7672, Lasos, Germany), with the wavelength of 633 nm and a beam diameter of 0.75 mm. The second source with a semiconductor laser (Obis 785 LX, Coherent, USA) with the wavelength of 780 nm and a beam diameter of 0.6 mm. The transmitted light was detected by a photodetector (Thorlabs 120 C, Thorlabs, USA) using a setup described in [20].

The total forward transmittance (TFT) of selected samples was measured with a double-beam spectrophotometer (Specord 250 Plus, Analytik Jena AG, Germany). The spectrophotometer was equipped with an integrating sphere with a spherical diameter of 75 mm. The measurement was repeated three times for each sample in the wavelength range between 300 nm and 900 nm; then, the arithmetical average and 95% confidence interval (t-distribution) of transmittance were calculated.

μ-Raman measurements were performed on the surface of sintered samples using a Raman microscope spectrometer (inVia Qontor, Reinshaw, UK) at room temperature, using 532 nm excitation wavelength. The spectra were collected from the center of the discs for wavenumbers between 200 and $1800\,cm^{-1}$. The background of the recorded spectra was removed using a polynomial function, and the spectra were normalized to the total area. The peaks located at ca. $1350\,cm^{-1}$ and $1600\,cm^{-1}$, associated with carbon D-band, were used to evaluate carbon contamination in samples.

Vickers indentation was performed using a maximum load of 19.61 N

Table 1
Specific surface area, particle size, and main impurities of used spinel powders.

Powder	SSA (m^2g^{-1})	Particle Size, d_{50} (μm)	Main impurities (ppm)					
			S	Fe	Na	Si	Ca	K
S25CR	23.3	0.20–0.30	200	10	50	30	45	50
S30CR	29.0	0.15–0.30	600	15	70	30	60	60

and 10 s holding time to measure the hardness of samples; the indentations were produced in ambient air (T = 20 °C and relative humidity 45%); at least 16 indentations were performed for each sample.

Phase analysis was performed by X-ray powder diffraction (Empyrean, Malvern Panalytical, The Netherlands) using CoK-α radiation. The surface microstructure of samples used for TFT measurement was examined using scanning electron microscopy (JSM-7600 F, JEOL, Japan).

The microstructure of selected samples was further analyzed by bright-field transmission electron microscopy (BF-TEM) performed on an FEI Talos F200S operating at 200 kV; small sections were cut from the center of sintered bodies prepared from pure S25CR and S25CR doped with 0.6 wt% LiOH and densified by using the "Fast" sintering schedule.

3. Results

The SPS schedule producing the highest light transmittance was determined by performing various combinations of heating rates and dwell time following the Sequential Design of Experiment (SDoE) approach. S30CR powder with no additives was used to produce reference samples; the samples were polished and the RIT at 633 nm was measured. Considering the RIT results, two SPS programs representing *Slow* (S) and *Fast* (F) were selected for further investigations:

(i) the *Slow* (S) schedule consists of a 100 °C/min heating till 1100 °C, where a slow heating rate of 2.75 °C.min^{-1} was applied until the sintering temperature of 1250 °C was achieved. No dwell time was applied. A constant pressure of 80 MPa was applied above 800 °C.

(ii) in the *Fast* (F) schedule, the samples were heated at 100 °C.min^{-1} to 1200 °C and, afterward, the temperature was increased to 1300 °C at 50 °C.min^{-1}; then, an isothermal step was applied for 3 min. A constant pressure of 80 MPa was applied above 1200 °C.

Fig. 1 shows the dependency of temperature, pressure, as well as punch displacement as a function of time for samples subjected to both SPS schedules (S): Fig. 1a, and (F): Fig. 1b. The displacement of punches during the schedule (S) contained two main regions: a fast shrinkage during the initial heating (heating rate of 100 °C/min) between 650 °C and 1100 °C upon the application of pressure (80 MPa), and a significantly slower shrinkage when the heating rate decreased to 2.75 °C. min^{-1}. The punch displacement reached the plateau above 1150 °C. Although the sintering shrinkage of samples was negligible above 1100 °C, it is reported that heating up to 1250 °C is necessary to sinter the discs homogenously and obtain transparent MgAl$_2$O$_4$ [12,19,21]. Also, the plateau in a piston movement can still mean that the densification proceeds; the densification of the sample can be compensated by the thermal expansion of the whole sintering setup during a long heat treatment. Fig. 1b shows the temperature and punch displacement during SPS using the schedule (F). The punch displacement was characterized by three different regions. A shrinkage between 600 °C and 900 °C was attributed to the rearrangement of particles under the initially applied pressure (5 MPa) [32]. In the second region, a small thermal expansion of the sintering disc was recorded up to 1000 °C. In the third region, the sample shrank rapidly after the applied pressure increased to 80 MPa and showed two different shrinkage rates: slower one as an initial shrinkage between 1200 °C and 1300 °C corresponding to the densification of the powder compact and a slightly faster shrinkage after the isothermal dwell at 1300 °C. The activation of the slip mechanisms and the densification via dislocation movement at high temperatures might be responsible for the increase of the shrinkage rate above 1300 °C [4,27,33].

The S25CR and S30CR powders doped with 0, 0.3 and 0.6 wt% LiOH were sintered using the schedules (S) and (F) as the optimal schedules based on RIT analyses. Table 2 summarizes the final density and real in-line transmission of samples produced by different SPS schedules. All the sintered discs exhibited a relative density larger than 99.7% of the theoretical density (3.58 g.cm^{-3}), indicating that the pores were almost completely eliminated at both sintering schedules. Despite the expected higher sinterability due to the relatively smaller particle size of the S30CR powder, the discs produced from the S30CR powder showed a slightly lower relative density than the S25CR samples. The addition of 0.3 wt% LiOH resulted in an increase in relative density, while the addition of 0.6 wt% LiOH led to a decrease in the relative density of samples. The discs sintered using the (F) schedule showed a slightly higher density compared to (S) schedule. However, the sample produced from S25CR powder doped with 0.3 wt% LiOH using (S) sintering schedule and those produced from S30CR powder doped with 0.3 wt% LiOH and densified by (F) schedule exhibited the highest density.

Fig. 2 shows the appearance of polished samples; sintered discs had a nominal thickness of 0.80 mm and were placed directly over the background. The samples produced from S30CR using the SPS (F) schedule
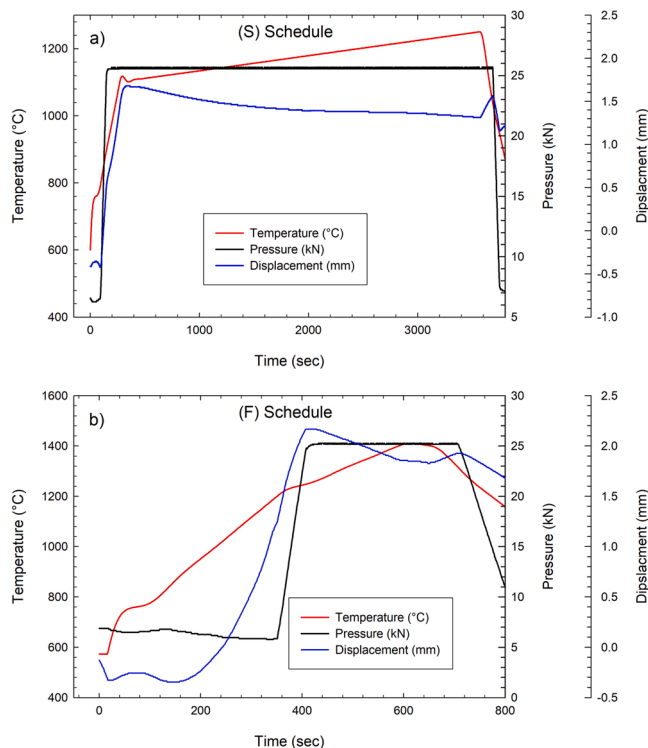

Fig. 1. Temperature and piston displacement for a) slow (S) and b) fast (F) sintering schedules. Plots show real records during SPS of S25CR powder with no LiOH additive.

Table 2
Abbreviation, LiOH concentration and Real In-line Transmission (RIT, determined at wavelengths of 633 and 780 nm).

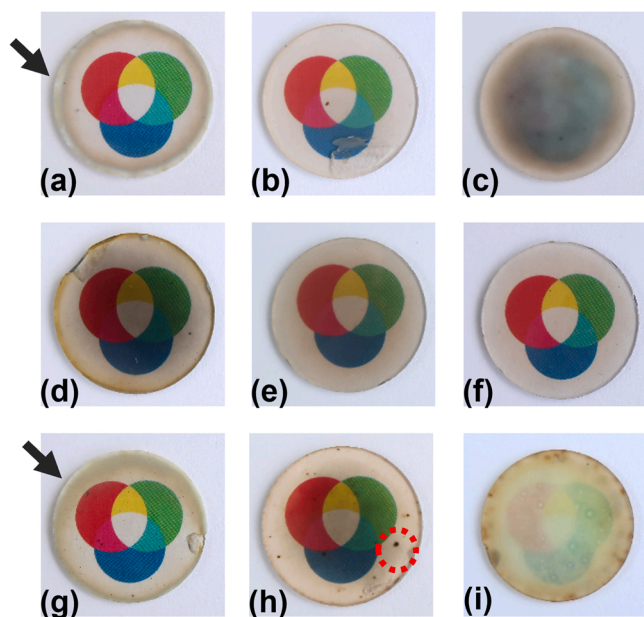| Heating schedule	Raw powder	LiOH (wt%)	Relative density (% t. d.)	RIT	
				633 nm (%)	780 nm (%)
Slow - (S)	S25CR	0.0	99.73 ± 0.03	84.8	84.1
		0.3	99.94 ± 0.07	46.8	45.5
		0.6	99.77 ± 0.06	16.3	30.1
	S30CR	0.0	99.72 ± 0.07	80.6	81.0
		0.3	99.74 ± 0.06	74.6	83.3
		0.6	99.75 ± 0.05	35.6	30.7
Fast - (F)	S25CR	0.0	99.84 ± 0.06	54.6	64.1
		0.3	99.88 ± 0.08	76.5	79.5
		0.6	99.82 ± 0.07	72.4	72.0
	S30CR	0.0	99.75 ± 0.08	-	-
		0.3	99.94 ± 0.11	-	-
		0.6	99.83 ± 0.06	-	-

Fig. 2. Optical photographs of samples (0.8 mm thickness) placed directly over the background produced from S25CR and S30CR powders doped by different amounts of LiOH.

were opaque and not transparent to the naked eye; thus, they were excluded from the RIT measurements. The rest of the samples were transparent except for the sample produced from S25CR doped with 0.6 wt% LiOH using the program (S), which was almost opaque with a brown/black color. Discs produced from undoped powders and sintered using schedule (S) were characterized by opaque edges, marked by arrows in Fig. 2a and g, indicating inhomogenous densification [19,34]. The undoped S25CR samples produced using SPS (F) schedule show a dark/black center. Such blackening of spinel bodies produced by SPS is attributed to carbon contamination [12,14,16]. There were small black dots inside the sample produced from the S30CR powder doped with 0.3 wt% of LiOH; a typical black spot is marked by a circle in Fig. 2h. These black spots are likely to be related to the introduced impurities during the powder treatment and are not associated with the sintering schedule.

Surface roughness of polished samples after SPS was also studied: the surface roughness affects the optical properties of samples (e.g. surface reflectivity) significantly. It is worth mentioning that the samples with higher carbon contamination (e.g. Fig. 2d) exhibited a larger roughness than the samples with lower carbon content ("carbon-free"). The carbon contaminated samples were characterized by the average Ra and Rz roughness parameters of 8.0 ± 2.0 nm and 110.0 ± 10.0 nm, whereas the average Ra= 0.7 ± 0.1 nm and Rz= 7.0 ± 4.0 nm were determined for "carbon-free" samples. Otherwise, no differences were found in samples with different compositions or densified using different sintering schedules; difference in roughness was thus attributed to carbon contamination.

The results of RIT measurements of the selected discs shown in Fig. 2 are summarized in Table 2. The discs produced from pure S25CR and sintered using the schedule (S) showed a slightly higher transmission than S30CR (84% vs. 80%). The real in-line transmittance for samples prepared from the S30CR powder doped with 0.3 wt% LiOH was ca. 75% and 83% at 633 nm and 780 nm, respectively, while the RIT of the samples from S25CR powder doped with 0.3 wt% LiOH was only about 46%. The samples containing 0.6 wt% LiOH and sintered using the heating schedule (S) showed a significantly lower RIT. In contrast, the RIT of discs produced by SPS using the schedule (F) increased significantly when the spinel powder was doped with 0.3 wt% LiOH (i.e., from ca. 55% to ca. 77% at the laser wavelength of 633 nm). The addition of

0.6 wt% LiOH resulted in a slight decrease in RIT of the samples sintered with the schedule (F). The overview of the RIT of individual samples and its dependencies is shown in Fig. 3. The effect of LiOH on the optical properties of magnesium-aluminate spinel is influenced by the sintering schedule. The addition of LiOH has a negative impact on the optical properties of spinel ceramics sintered by a schedule that exposes the sample to high temperatures for a relatively long time, i.e. using a slow heating rate (as in the (S) schedule).

Fig. 4 shows the hardness of the samples produced from S25CR using sintering schedules (F) and (S) as a function of LiOH content. The Vickers hardness varies between 13 and 16 GPa which is comparable to the reported values for transparent magnesium aluminate spinel bodies with submicron grain size [35,36]. The samples sintered using the (S) schedule are characterized by a higher hardness than those prepared by the (F) schedule. Moreover, the addition of LiOH decreases the hardness of spinel samples.

Fig. 5 shows the polished surface of the samples produced from S25CR using the sintering schedule "F". The samples were ground to half of their thickness and polished to reveal the residual pores or contamination within the core of the samples. The samples doped with LiOH were homogenously dense; the polishing scratches were the only visible feature of the samples, and no porosity was observed. The additive-free samples (Fig. 5a) were characterized by the presence of grain pull-outs and few isolated pores, which might be related to inhomogeneous densification or the presence of carbon residues due to the contamination during spark plasma sintering. The inhomogeneous densification of samples accounts for fluctuations in mechanical properties. Although the origin of such peculiar microstructural singularities is not clear, they might act as scattering centres, disperse light and cause the opaqueness of the sample. Further studies are required to understand the mechanical and fractographic response of transparent spinel ceramics [37].

The contamination of samples with carbon was examined by Raman spectroscopy. The measured μ-Raman spectra are depicted in Fig. 6. The corrected μ-Raman spectra collected over the center of discs (as is shown in Fig. 2) revealed carbon or graphite peaks between 1250 and 1750 cm^{-1}. The S25CR sample sintered using the schedule (S) showed two major peaks at 1350 cm^{-1} and 1600 cm^{-1} (Fig. 6a) that are respectively attributed to the D and D′-bands of amorphous carbon or graphite oxide [38]. This indicates that the carbon contamination occurred through the reaction between the powder and the graphite die. Conversely, the S25CR sample doped with 0.6 wt% shows a peak at ca. 1580 cm^{-1} that is attributed to the ordered carbon in the graphite structure [39]. The presence of graphite in sintered discs indicates that the powder was contaminated by debris from the graphite die or graphite paper used for SPS, which is responsible for the poor
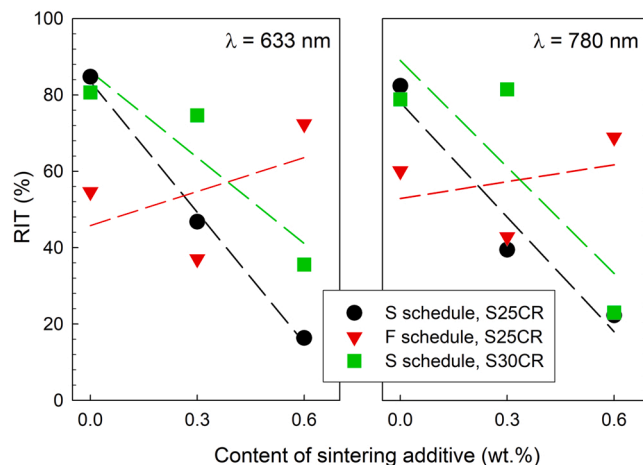

Fig. 3. Dependence of RIT on the sintering schedule, content of sintering additive and wavelength of used laser.
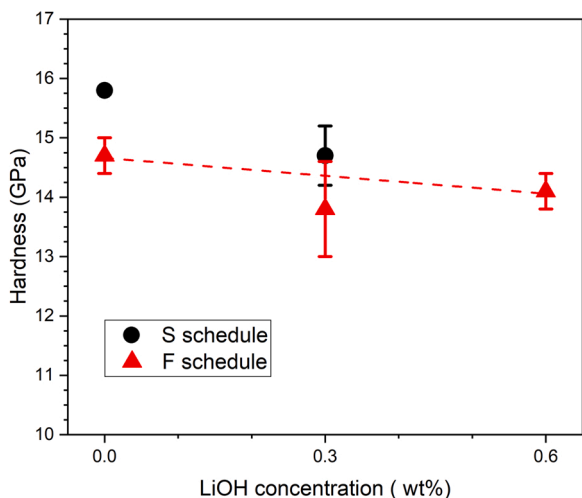
Fig. 4. Vickers hardness of samples produced from S25CR doped with LiOH using "F" and "S" sintering schedules (with dashed line as a guide to the eye).

transparency of the sample. The additive-free S25CR powder showed the highest carbon contamination among the discs sintered using the schedule (F). The addition of 0.3 wt% LiOH suppressed the carbon contamination in the sample (see microstructure in Fig. 5). The increase of LiOH addition to 0.6 wt% LiOH further reduced carbon contamination.

Although the LiOH-free S30CR disc sintered by the schedule (S) showed high-intensity carbon peaks, the carbon contamination in the LiOH-doped samples was reduced, and the concentration of carbon was below the detection limit of the collected Raman spectra.

The overall transparency was further investigated by determining the total forward transmission (TFT) of the samples produced from the S25CR powder. The three following samples were selected for TFT measurements: additive-free and 0.3 wt% LiOH doped sample sintered using the schedule (S), and the 0.6 wt% LiOH doped sample sintered using the schedule (F). The average total forward transmittance is shown in Fig. 7; tint-colored lines represent 95% confidence interval (t-distribution).

4. Discussion

The results of RIT analyses and optical photographs are summarized in Table 2, Figs. 2 and 3. Theoretically, higher RIT is expected at longer wavelengths [23]. However, the results of RIT measurements are

Fig. 5. SEM micrographs of samples produced using "S" sintering schedule form S25CR doped with various concentrations of LiOH (a) additive free, (b) 0.3 wt% LiOH, and (c) 0.6 wt% LiOH.
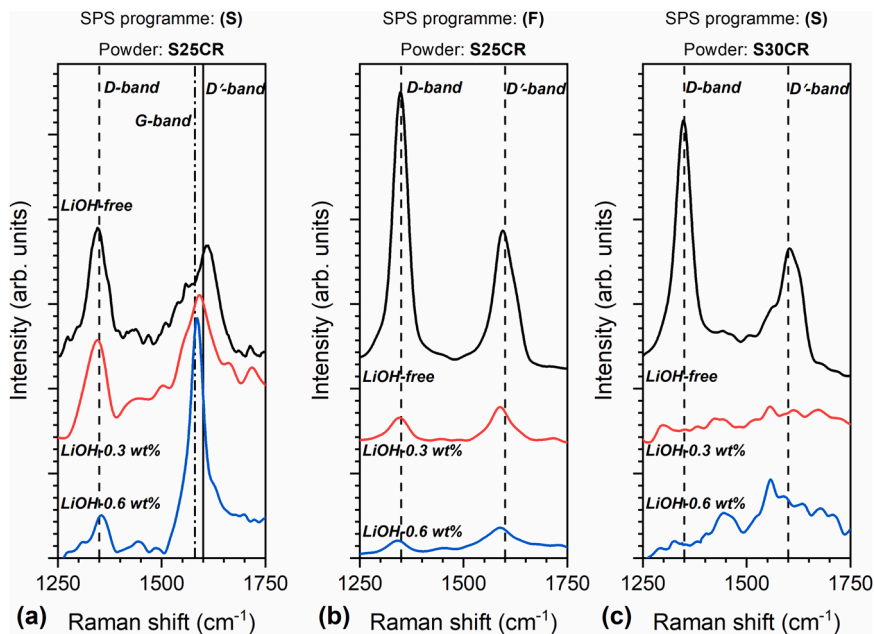

Fig. 6. μ-Raman spectra collected from the centre of discs: a) and b) spectra of samples from S25CR powder sintered using the schedules (S) and (F), respectively; c) spectra of samples from S30CR powder sintered using (S) schedule.
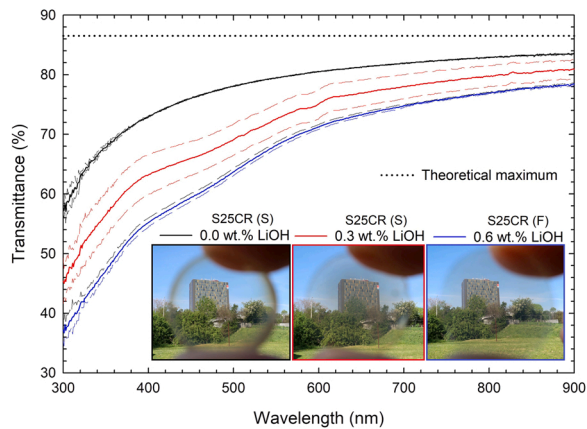
Fig. 7. Total forward transmission of selected samples produced from S25CR powder and sintered using different SPS schedules. The dotted line presents the maximal conceivable transmittance for $MgAl_2O_4$, dashed lines represent 95% confidence intervals.

Fig. 8. RIT of selected transparent $MgAl_2O_4$ samples produced from S30CR using SPS in this study and compared to RIT values with samples from literature (please note, that the samples from literature have a thickness from 0.8 to 1.0 mm) [9,23,25,33,36,41,42]. The difference between various sintering aids (LiOH or LiF) and concentrations are determined by a different symbol; the size of symbols corresponds to the heating rate of SPS (i.e. bigger symbol size, the higher heating rate). The dashed line serves as reader's eye guide to follow the impact of sintering temperature.

scattered and the transmittance decreases when a higher wavelength is used (Fig. 2). Moreover, the results of RIT measurements are different from the TFT measurements. Although the RIT experiments were repeated to improve the precision of the results, the measurement values remained scattered; performing the measurement on various parts of samples due to the use of a narrow beam might be responsible for the scattered results. Nevertheless, the trends in transmittance remain the same for both RIT and TFT measurements. The RIT measurements thus represent a valid option for the comparison between individual samples.

The results of this study indicate that the addition of limited amounts of LiOH can be beneficial to the fabrication of magnesium aluminate spinel using a high heating rate and short time SPS (the (F) schedule), particularly by suppressing carbon contamination. Previous works reported on the effects of SPS schedule on transparency and carbon contamination in spinel ceramics [12,13,17,18]. Decreasing the heating rate after "critical temperature" reduces the carbon contamination and improves the translucency of spinel; for samples without additives, the slow heating rate led to the highest RIT transparency of 84.8% at 633 nm. However, the slow heating of samples makes the SPS process lengthy [18,19]. Thus, alternative energy-conserving SPS programs shall be pursued. Another approach is to apply the highest pressure after a specific temperature, which is reported to enhance the transparency of spinel discs [29]. Although the findings of this study are in line with previously published results [19,29], increasing the applied pressure is less effective for the samples produced from S30CR powder.

None of the explanations of the mechanism of carbon contamination during SPS of oxide ceramics is conclusive. Nonetheless, the impact of LiOH doping on the densification of spinel is responsible for the changes in carbon contamination and, in turn, the transparency of samples. It has been pointed out that performing SPS at a lower temperature makes the thermodynamic conditions for carbon deposition inside the pores less favorable [3,14,19,40]. Doping magnesium aluminate spinel with LiOH significantly reduces the activation energy of sintering [26], which enables pores elimination and obtaining a highly dense body at a lower temperature. As a consequence, LiOH addition prevents carbon contamination.

Fig. 8 compares the RIT of LiOH-doped samples in this study with typical RIT reported for the spinel samples doped with LiF as the sintering aid. The RIT of the sample doped with 0.3 wt% LiOH and sintered using the slow heating schedule is higher than the samples doped with LiF. Unlike LiF, which is conventionally used as a sintering aid, LiOH produces no liquid phase and, therefore, there is no loss in the transparency of spinel discs doped with LiOH due to light scattering by residual phases at grain boundaries and in triple grain boundary junctions [19,21,22,41]. However, the RIT of the samples doped with 0.6 wt%
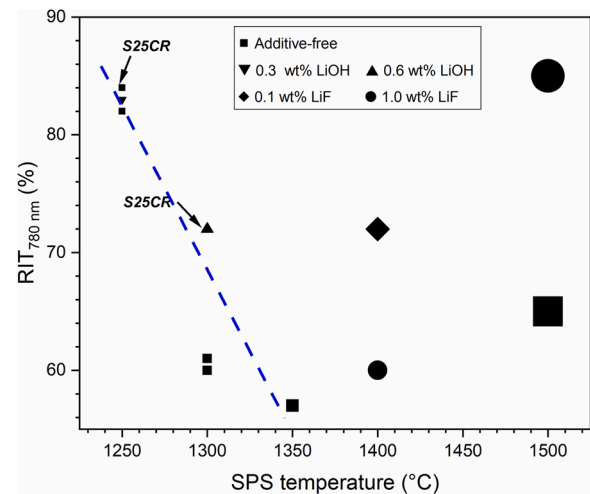
LiOH and consolidated at a high heating rate is significantly lower than the RIT of the samples doped with LiF. The results obtained in this work indicate that, in terms of RIT, the slow sintering is not favorable for doped samples. During the slow heating schedules, the samples are subjected to high temperatures for a longer time. The Li^+ ions incorporated into the spinel structure precipitate above 1040 °C and produce $LiAlO_2$ [26]. The precipitated particles act as scattering centres at grain boundaries, reducing the transmission. [27].

Nevertheless, comparing the RIT of the samples produced in this study with other studies (Fig. 8), it can be concluded that doping with LiOH is at least as effective as doping with LiF. Moreover, the samples can be sintered at much lower temperatures.

Fig. 9 shows the X-ray diffraction patterns of samples produced from S25CR powder and sintered using the schedule (F). While LiOH-free samples and the samples doped with 0.3 wt% show the characteristic reflections only corresponding to magnesium-aluminate spinel, small diffraction maxima corresponding to secondary phases such as $LiAlO_2$ can be observed in the XRD pattern of the sample containing 0.6 wt% LiOH. It has been shown that the reaction between lithium oxide, formed by the decomposition of LiOH, and spinel $(MgAl_2O_4)$, produces MgO and $LiAlO_2$ [26,43]. The secondary phases, whose refractive index differs from the matrix, act as scattering centers and reduce light transmission [15]. The refractive indices of MgO, $MgAl_2O_4$ (spinel), and $LiAlO_2$ at 600 nm are 1.73, 1.71, and 1.65 [44], respectively. Please note that these refractive indices are theoretical values calculated using the density functional theory.

Light wave may reflect at the interface of phases with different refractive indices. The reflected wave bends away from an optically denser structure (i.e. with high refractive index, MgO) toward optically thinner structure (i.e of low refractive index, spinel). Such change in the traveling direction of the light wave results in a decrease in light intensity. Eventually the light intensity is extinct before it can leave the material (e.g. due to absorption or more pronounced internal reflection). The situation is even more complex in the case of $LiAlO_2$ dispersed in a spinel matrix since the secondary phase is birefringent. $LiAlO_2$ has a tetragonal crystallographic lattice; thus, the incident wave is split into two waves (ordinary and extraordinary wave). Each wave is polarised with vibration directions mutually perpendicular to one another and traveling at different velocities. The ordinary and extraordinary
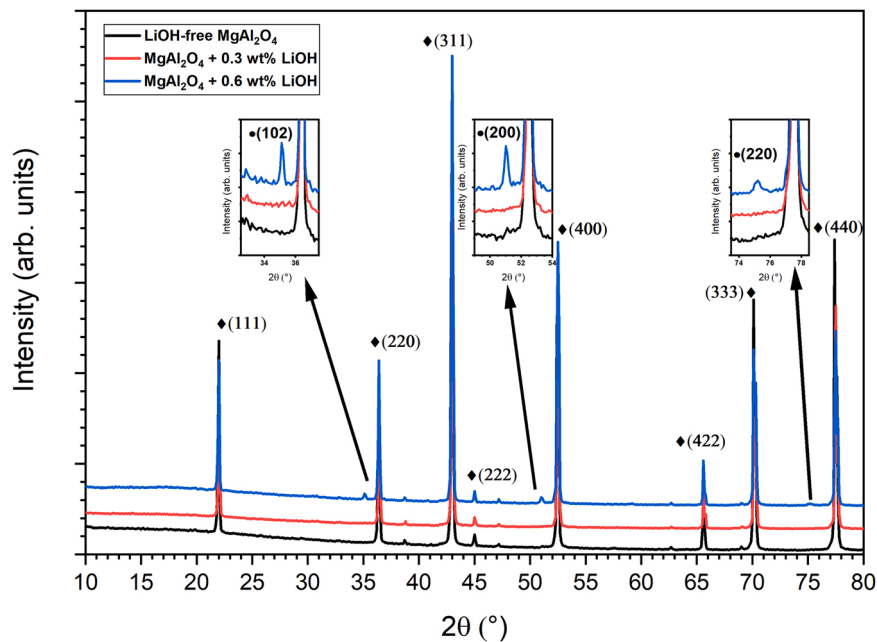
Fig. 9. XRD patterns of samples comprising S25CR and 0.0, 0.3 and 0.6 wt% of LiOH at room temperature after Spark Plasma Sintering using the (F) schedule. The insets magnify the less visible peaks: (◆: $MgAl_2O_4$ Spinel, •: $LiAlO_2$).

refractive indices of $LiAlO_2$ at 633 nm are $n_o = 1.6197$ and $n_e = 1.6014$, respectively [45]. The refractive index difference of the secondary phase $LiAlO_2$ is relatively small and is equal to $\Delta n = n_e - n_o = -0.0183$. This means that the uniaxial birefringence of $LiAlO_2$ is negative and, therefore, the polarised extraordinary wave is parallel to optical axis. Thus, the $LiAlO_2$ as a secondary phase acts more probably as a scattering centre. However, given the small difference in reflective indices of phases, substantial amounts of $LiAlO_2$ must be present to impair the transparency.

At temperatures above 1200 °C, $LiAlO_2$ and MgO react back into spinel ($MgAl_2O_4$) [26]. However, the short exposure of samples sintered using the fast (F) schedule to high temperatures results only in a partial reaction of MgO and $LiAlO_2$; the residual phases (MgO and $LiAlO_2$) will thus deteriorate the transparency.

The maximal transmittance, T^{max}, can be calculated from the refractive index n using the following equation: $T^{max} = 2 \cdot n \, / \, (n^2 + 1) \cdot 100$. As spinel represents the matrix, the refractive index of spinel ($n = 1.71$) was used to estimate $T^{max}_{n=1.71}$, which is 87.15% at 633 nm, and approximated this value to the whole wavelength range (see the dotted line in Fig. 7). This is a conservative estimate since the refractive index is wavelength dependent. However, we believe such an approximation is accurate enough to simulate and explain the cause of the changes in the transparency of samples in this study. The transmittance values obtained experimentally by spectrophotometry with integrating sphere for samples S25CR with the slow heating schedule without LiOH additive, with 0.3 wt% and 0.6 wt% of LiOH additive, are $81.0 \pm 0.0\%$, $76.5 \pm 2.3\%$ and $72.7 \pm 0.4\%$, respectively. Using the calculated T^{max} value equal to 87.15%, the transmittance of about 93%, 88% and 83% of the theoretical maximum was achieved.

The samples from S25CR powder sintered by (S) schedule doped with 0.3 and 0.6 wt% of LiOH showed a lower total forward transmittance than the additive-free sample despite the fact it is characterised by the highest density among the produced samples. Moreover, while the TFT results of the samples doped with 0.6 wt% LiOH and additive-free samples showed high reproducibility (a narrow confidence interval), the sample doped with 0.3 wt% LiOH is characterized by scattered TFT values. The scattering of light by secondary particles with various radii might be responsible for such behavior [46] which implies that the additive was inhomogeneously mixed with spinel power during powder

processing.

An interesting aspect of the results obtained in this study is that, despite very similar characteristics of the used powders, the influence of LiOH addition on the transparency depends on the source of the spinel. There are two main differences between the powders: the concentration of sulfur impurity of S30CR is higher than S25CR, and its particle size is smaller (Table 1). The reaction between the fluoride sintering aids, such as LiF in $MgAl_2O_4$, yields a liquid phase that can scavenge the impurities, such as sulfates, and remove them from the system at lower temperatures [20,24]. However, the reaction of lithium oxide, produced by the thermal decomposition of LiOH, with impurities might result in the formation of phases that cannot be removed at lower temperatures. Subjecting the samples to high temperatures is thus necessary to remove the impurities. The S30CR contains a larger amount of impurities and, thus, sintering for a shorter time (the (F) schedule) produces opaque samples. One final note concerns the peculiar decrease of the transparency of samples with the addition of LiOH (Fig. 3). While the samples produced from S30CR doped with 0.3 wt% LiOH exhibited almost similar RIT as the undoped samples, adding 0.3 wt% LiOH to S25CR resulted in a dramatic decrease. It has been reported that there is a critical concentration of lithium ions above which the incorporation mechanism of Li^+ into $MgAl_2O_4$ structure changes and thus influences the formation of secondary phases [26,47]. Thus, one might expect that the critical concentration of Li^+ in polycrystalline spinel is a function of particle size. Therefore, the critical Li^+ concentration for S25CR powder is expected to be smaller than for S30CR due to its smaller surface area. However, further microstructural studies are necessary to identify the secondary phases that significantly impact the transparency of LiOH-doped spinel bodies.

Although using LiOH as a sintering aid improves the densification of $MgAl_2O_4$ and enables the fabrication of transparent bodies in a short time, the samples doped with LiOH exhibited lower hardness values compared to the pure ones. Fig. 10 shows the BF-TEM micrographs taken from the samples produced from LiOH-free S25CR and the powder doped with 0.6 wt% LiOH; the samples were fabricated following the fast-sintering schedule (F) with a holding temperature of 1300 °C. The LiOH-free sample is characterized by smaller grains than the sample doped with 0.6 wt% LiOH (230 ± 85 nm vs. 460 ± 150 nm). It is reported that the incorporation of Li^+ ions into the $MgAl_2O_4$ structures
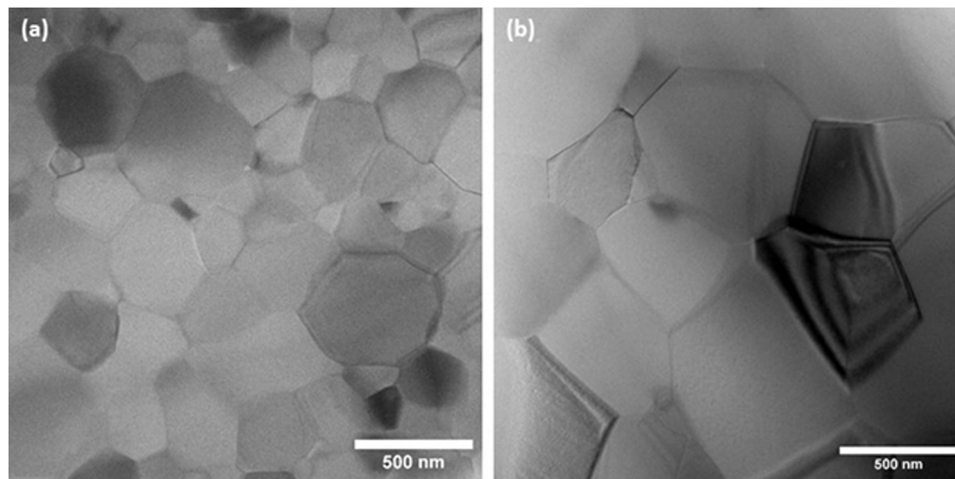
Fig. 10. BF-TEM images of samples produced from S25CR powder using "Fast" sintering schedule; (a) additive-free S25CR, and (b) S25CR+ 0.6 wt% LiOH.

increases the concentration of oxygen vacancies and, in turn, improves the diffusion processes; this promotes densification and grain growth. However, there is an expected critical concentration of lithium ions above which grain growth occurs [26,47,48]. Nevertheless, despite the effect of LiOH on grain growth, it improves the transparency of samples produced by the fast sintering schedule (F).

Sokol et al. studied the influence of microstructural features of transparent $MgAl_2O_4$ bodies (produced from a powder with similar characteristics as our powders) on their hardness and flexural strength [35,49]. They observed that the flexural strength of samples was strongly affected by the grain size; the dependence of the flexural strength σ_{fl}, on the grain size, D, can be expressed as:

$$\sigma_{fl} = \sigma_{fl}^0 + \frac{a}{\sqrt{D}} \tag{1}$$

where σ_{fl}^0 is a constant, and a is the slope representing the grain size dependence of flexural strength. The slope was reported to be about 4×10^{-2} MPa m$^{0.5}$ for samples with a grain size smaller than 4 μm [35]. Considering the grain size of the samples in Fig. 10 and Eq. (1), it is expected that the flexural strength of Li-doped samples is by ca. 24 MPa lower than the strength of the ones sintered without additives. This shows that the influence of grain growth caused by LiOH addition on mechanical properties is negligible. However, more studies are required to understand how LiOH affects the mechanical properties of transparent $MgAl_2O_4$.

5. Conclusion

Transparent magnesium aluminate spinel was produced from commercial powders differing in specific surface area and the content of impurities (especially sulfur) by spark plasma sintering using different heating schedules. The transparency of spinel ceramics was simultaneously influenced by the powder properties and the sintering schedule. Although slow heating from 1100 °C to 1250 °C at 2.75 °C/min with no dwell enabled the preparation of samples transparent in the centre from both powders, the densification was inhomogeneous at the edges. Fast heating to 1300 °C and 3 min isothermal dwell yielded homogenously sintered transparent bodies. Fast heating was not applicable to the powder with higher specific surface area, i.e. the powder with finer particles. The addition of LiOH resulted in homogenous densification of $MgAl_2O_4$; however, its effect on the transparency of samples is not straightforward and is more influenced by the sintering schedule.

Declaration of Competing Interest

The authors declare that they have no known competing financial interests or personal relationships that could have appeared to influence the work reported in this paper.

Acknowledgements

References

[1] M. Sokol, B. Ratzker, S. Kalabukhov, M.P. Dariel, E. Galun, N. Frage, Transparent polycrystalline magnesium aluminate spinel fabricated by spark plasma sintering, Adv. Mater. 30 (2018) 1706283, https://doi.org/10.1002/adma.201706283.

[2] I. Ganesh, A review on magnesium aluminate (MgAl2O4) spinel: synthesis, processing and applications, Int. Mater. Rev. 58 (2013) 63–112, https://doi.org/10.1179/1743280412Y.0000000001.

[3] I. Reimanis, H.-J. Kleebe, A review on the sintering and microstructure development of transparent spinel (MgAl2O4), J. Am. Ceram. Soc. 92 (2009) 1472–1480, https://doi.org/10.1111/j.1551-2916.2009.03108.x.

[4] M.R. du Merac, H.-J. Kleebe, M.M. Müller, I.E. Reimanis, Fifty years of research and development coming to fruition; unraveling the complex interactions during processing of transparent magnesium aluminate (MgAl2O4) spinel, J. Am. Ceram. Soc. 96 (2013) 3341–3365, https://doi.org/10.1111/jace.12637.

[5] L. Lallemant, G. Fantozzi, V. Garnier, G. Bonnefont, Transparent polycrystalline alumina obtained by SPS: Green bodies processing effect, J. Eur. Ceram. Soc. 32 (2012) 2909–2915, https://doi.org/10.1016/j.jeurceramsoc.2012.02.041.

[6] S. Hříbalová, W. Pabst, Light scattering in monodisperse systems – from suspensions to transparent ceramics, J. Eur. Ceram. Soc. 40 (2020) 1522–1531, https://doi.org/10.1016/j.jeurceramsoc.2019.11.053.

[7] S. Hříbalová, W. Pabst, Light scattering and extinction in polydisperse systems, J. Eur. Ceram. Soc. 40 (2020) 867–880, https://doi.org/10.1016/j.jeurceramsoc.2019.10.054.

[8] R. Chaim, R. Marder, C. Estournès, Optically transparent ceramics by spark plasma sintering of oxide nanoparticles, Scr. Mater. 63 (2010) 211–214, https://doi.org/10.1016/j.scriptamat.2010.03.056.

[9] K. Morita, B.-N. Kim, K. Hiraga, H. Yoshida, Fabrication of transparent MgAl2O4 spinel polycrystal by spark plasma sintering processing, Scr. Mater. 58 (2008) 1114–1117, https://doi.org/10.1016/j.scriptamat.2008.02.008.

[10] S. Bhaduri, S.B. Bhaduri, Microstructural and mechanical properties of nanocrystalline spinel and related composites, Ceram. Int. 28 (2002) 153–158, https://doi.org/10.1016/S0272-8842(01)00071-2.

[11] A. Goldstein, J. Raethel, M. Katz, M. Berlin, E. Galun, Transparent MgAl2O4/LiF ceramics by hot-pressing: Host–additive interaction mechanisms issue revisited, J. Eur. Ceram. Soc. 36 (2016) 1731–1742, https://doi.org/10.1016/j.jeurceramsoc.2016.02.001.

[12] K. Morita, B.-N. Kim, H. Yoshida, K. Hiraga, Y. Sakka, Influence of spark plasma sintering (SPS) conditions on transmission of MgAl2O4 spinel, J. Am. Ceram. Soc. 98 (2015) 378–385, https://doi.org/10.1111/jace.13309.

[13] K. Morita, B.-N. Kim, H. Yoshida, K. Hiraga, Y. Sakka, Assessment of carbon contamination in MgAl2O4 spinel during spark-plasma-sintering (SPS) processing, J. Ceram. Soc. Jpn. 123 (2015) 983–988, https://doi.org/10.2109/jcersj2.123.983.

[14] P. Wang, Z. Huang, K. Morita, Q. Li, M. Yang, S. Zhang, T. Goto, R. Tu, Influence of spark plasma sintering conditions on microstructure, carbon contamination, and transmittance of CaF2 ceramics, J. Eur. Ceram. Soc. 42 (2022) 245–257, https://doi.org/10.1016/j.jeurceramsoc.2021.10.004.

[15] S. Hříbalová, W. Pabst, Theoretical study of the influence of carbon contamination on the transparency of spinel ceramics prepared by spark plasma sintering (SPS), J. Eur. Ceram. Soc. 41 (2021) 4337–4342, https://doi.org/10.1016/j.jeurceramsoc.2021.01.036.

[16] K. Morita, B.-N. Kim, H. Yoshida, K. Hiraga, Y. Sakka, Spectroscopic study of the discoloration of transparent MgAl2O4 spinel fabricated by spark-plasma-sintering (SPS) processing, Acta Mater. 84 (2015) 9–19, https://doi.org/10.1016/j.actamat.2014.10.030.

[17] K. Morita, B.-N. Kim, H. Yoshida, K. Hiraga, Y. Sakka, Distribution of carbon contamination in oxide ceramics occurring during spark-plasma-sintering (SPS) processing: II - Effect of SPS and loading temperatures, J. Eur. Ceram. Soc. 38 (2018) 2596–2604, https://doi.org/10.1016/j.jeurceramsoc.2017.12.004.

[18] K. Morita, B.-N. Kim, H. Yoshida, K. Hiraga, Y. Sakka, Distribution of carbon contamination in MgAl2O4 spinel occurring during spark-plasma-sintering (SPS) processing: I – Effect of heating rate and post-annealing, J. Eur. Ceram. Soc. 38 (2018) 2588–2595, https://doi.org/10.1016/j.jeurceramsoc.2017.09.038.

[19] A. Talimian, V. Pouchly, H.F. El-Maghraby, K. Maca, D. Galusek, Transparent magnesium aluminate spinel: Effect of critical temperature in two-stage spark plasma sintering, J. Eur. Ceram. Soc. 40 (2020) 2417–2425, https://doi.org/10.1016/j.jeurceramsoc.2020.02.012.

[20] A. Talimian, V. Pouchly, K. Maca, D. Galusek, Densification of magnesium aluminate spinel using manganese and cobalt fluoride as sintering aids, Materials 13 (2020) 102, https://doi.org/10.3390/ma13010102.

[21] K. Rozenburg, I.E. Reimanis, H.-J. Kleebe, R.L. Cook, Sintering kinetics of a MgAl2O4 spinel doped with LiF, J. Am. Ceram. Soc. 91 (2008) 444–450, https://doi.org/10.1111/j.1551-2916.2007.02185.x.

[22] M.R. du Merac, I.E. Reimanis, C. Smith, H.-J. Kleebe, M.M. Müller, Effect of impurities and LiF additive in hot-pressed transparent magnesium aluminate spinel, Int. J. Appl. Ceram. Technol. 10 (2013) E33–E48, https://doi.org/10.1111/j.1744-7402.2012.02828.x.

[23] V. Nečina, W. Pabst, Grain growth of MgAl2O4 ceramics with LiF and NaF addition, Open Ceram. 5 (2021) 100078, https://doi.org/10.1016/j.oceram.2021.100078.

[24] K. Rozenburg, I.E. Reimanis, H.-J. Kleebe, R.L. Cook, Chemical interaction between LiF and MgAl2O4 spinel during sintering, J. Am. Ceram. Soc. 90 (2007) 2038–2042, https://doi.org/10.1111/j.1551-2916.2007.01723.x.

[25] V. Nečina, W. Pabst, Comparison of the effect of different alkali halides on the preparation of transparent MgAl2O4 spinel ceramics via spark plasma sintering (SPS), J. Eur. Ceram. Soc. 40 (2020) 6043–6052, https://doi.org/10.1016/j.jeurceramsoc.2020.06.056.

[26] A. Talimian, H.F. El-Maghraby, M. Michálková, D. Galusek, Sintering and grain growth behaviour of magnesium aluminate spinel: Effect of lithium hydroxide addition, J. Eur. Ceram. Soc. 41 (2021) 5634–5643, https://doi.org/10.1016/j.jeurceramsoc.2021.05.003.

[27] Y. Mordekovitz, L. Shelly, M. Halabi, S. Kalabukhov, S. Hayun, The effect of lithium doping on the sintering and grain growth of SPS-processed, non-stoichiometric magnesium aluminate spinel, Materials 9 (2016) 481, https://doi.org/10.3390/ma9060481.

[28] B.-N. Kim, A. Dash, Y.-W. Kim, K. Morita, H. Yoshida, J.-G. Li, Y. Sakka, Low-temperature spark plasma sintering of alumina by using SiC molding set, J. Ceram. Soc. Jpn 124 (2016) 1141–1145, https://doi.org/10.2109/jcersj2.16082.

[29] C. Wang, Z. Zhao, Transparent MgAl2O4 ceramic produced by spark plasma sintering, Scr. Mater. 61 (2009) 193–196, https://doi.org/10.1016/j.scriptamat.2009.03.039.

[30] Y. Xiong, J. Hu, Z. Shen, V. Pouchly, K. Maca, Preparation of transparent nanoceramics by suppressing pore coalescence, J. Am. Ceram. Soc. 94 (2011) 4269–4273, https://doi.org/10.1111/j.1551-2916.2011.04829.x.

[31] A. Kocjan, M. Logar, Z. Shen, The agglomeration, coalescence and sliding of nanoparticles, leading to the rapid sintering of zirconia nanoceramics, Sci. Rep. 7 (2017) 2541, https://doi.org/10.1038/s41598-017-02760-7.

[32] R. Chaim, Densification mechanisms in spark plasma sintering of nanocrystalline ceramics, Mater. Sci. Eng. A 443 (2007) 25–32, https://doi.org/10.1016/j.msea.2006.07.092.

[33] P. Fu, W. Lu, W. Lei, Y. Xu, X. Wang, J. Wu, Transparent polycrystalline MgAl2O4 ceramic fabricated by spark plasma sintering: Microwave dielectric and optical properties, Ceram. Int. 39 (2013) 2481–2487, https://doi.org/10.1016/j.ceramint.2012.09.006.

[34] J.-H. Lee, B.-N. Kim, S. Hata, B.-K. Jang, Microstructural and spectroscopic analysis in non-uniform Y2O3 ceramics fabricated by spark plasma sintering, J. Ceram. Soc. Jpn. 129 (2021) 66–72, https://doi.org/10.2109/jcersj2.20173.

[35] M. Sokol, S. Kalabukhov, R. Shneck, E. Zaretsky, N. Frage, Effect of grain size on the static and dynamic mechanical properties of magnesium aluminate spinel (MgAl2O4), J. Eur. Ceram. Soc. 37 (2017) 3417–3424, https://doi.org/10.1016/j.jeurceramsoc.2017.04.025.

[36] A. Rothman, S. Kalabukhov, N. Sverdlov, M.P. Dariel, N. Frage, The effect of grain size on the mechanical and optical properties of spark plasma sintering-processed magnesium aluminate spinel MgAl2O4, Int. J. Appl. Ceram. Technol. 11 (2014) 146–153, https://doi.org/10.1111/j.1744-7402.2012.02849.x.

[37] D. Drdlik, K. Drdlikova, H. Hadraba, K. Maca, Optical, mechanical and fractographic response of transparent alumina ceramics on erbium doping, J. Eur. Ceram. Soc. 37 (2017) 4265–4270, https://doi.org/10.1016/j.jeurceramsoc.2017.02.043.

[38] K. Morita, B.-N. Kim, H. Yoshida, K. Hiraga, Y. Sakka, Spectroscopic study of the discoloration of transparent MgAl2O4 spinel fabricated by spark-plasma-sintering (SPS) processing, Acta Mater. 84 (2015) 9–19, https://doi.org/10.1016/j.actamat.2014.10.030.

[39] K.N. Kudin, B. Ozbas, H.C. Schniepp, R.K. Prud`homme, I.A. Aksay, R. Car, Raman spectra of graphite oxide and functionalized graphene sheets, Nano Lett. 8 (2008) 36–41, https://doi.org/10.1021/nl071822y.

[40] L. Esposito, A. Piancastelli, P. Miceli, S. Martelli, A thermodynamic approach to obtaining transparent spinel (MgAl2O4) by hot pressing, J. Eur. Ceram. Soc. 35 (2015) 651–661, https://doi.org/10.1016/j.jeurceramsoc.2014.09.005.

[41] W. Luo, R. Xie, M. Ivanov, Y. Pan, H. Kou, J. Li, Effects of LiF on the microstructure and optical properties of hot-pressed MgAl2O4 ceramics, Ceram. Int. 43 (2017) 6891–6897, https://doi.org/10.1016/j.ceramint.2017.02.110.

[42] M. Azizi-Malekabadi, R. Sarraf-Mamoory, Devising a novel method of producing high transparent magnesium aluminate spinel (MgAl2O4) ceramics body using synthesized LiF nanopowder and spark plasma sintering, Mater. Chem. Phys. 250 (2020), 123035, https://doi.org/10.1016/j.matchemphys.2020.123035.

[43] S. Meir, S. Kalabukhov, N. Froumin, M.P. Dariel, N. Frage, Synthesis and densification of transparent magnesium aluminate spinel by SPS processing, J. Am. Ceram. Soc. 92 (2009) 358–364, https://doi.org/10.1111/j.1551-2916.2008.02893.x.

[44] I. Petousis, D. Mrdjenovich, E. Ballouz, M. Liu, D. Winston, W. Chen, T. Graf, T. D. Schladt, K.A. Persson, F.B. Prinz, High-throughput screening of inorganic compounds for the discovery of novel dielectric and optical materials, Sci. Data 4 (2017), 160134, https://doi.org/10.1038/sdata.2016.134.

[45] B. Cockayne, B. Lent, The Czochralski growth of single crystal lithium aluminate, LiAlO2, J. Cryst. Growth 54 (1981) 546–550, https://doi.org/10.1016/0022-0248(81)90511-X.

[46] S. Hříbalová, W. Pabst, Modeling light scattering by spherical pores for calculating the transmittance of transparent ceramics – All you need to know, J. Eur. Ceram. Soc. 41 (2021) 2169–2192, https://doi.org/10.1016/j.jeurceramsoc.2020.11.046.

[47] A.A. Bernardes, L.B. Caliman, A.L. da Silva, J. Bettini, K.L. Guimarães, D. Gouvea, Li2O-doped MgAl2O4 nanopowders: energetics of interface segregation, J. Am. Ceram. Soc. 103 (2020) 2835–2844, https://doi.org/10.1111/jace.16942.

[48] L.B. Caliman, D. Muche, A. Silva, C.A. Ospina R, I.F. Machado, R.H.R. Castro, D. Gouvêa, Effect of segregation on particle size stability and SPS sintering of Li2O-Doped magnesium aluminate spinel, J. Eur. Ceram. Soc. 39 (2019) 3213–3220, https://doi.org/10.1016/j.jeurceramsoc.2019.04.017.

[49] M. Sokol, M. Halabi, Y. Mordekovitz, S. Kalabukhov, S. Hayun, N. Frage, An inverse Hall-Petch relation in nanocrystalline MgAl2O4 spinel consolidated by high pressure spark plasma sintering (HPSPS), Scr. Mater. 139 (2017) 159–161, https://doi.org/10.1016/j.scriptamat.2017.06.049.